nature materials

SUPPLEMENTARY INFORMATION

https://doi.org/10.1038/s41563-020-0635-6

In the format provided by the authors and unedited.

Realizing spin Hamiltonians in nanoscale active photonic lattices

Midya Parto[1,4], William Hayenga[1,4], Alireza Marandi[2], Demetrios N. Christodoulides[1] and Mercedeh Khajavikhan[1,3]✉

[1]CREOL, The College of Optics and Photonics, University of Central Florida, Orlando, FL, USA. [2]Department of Electrical Engineering, California Institute of Technology, Pasadena, CA, USA. [3]Ming Hsieh Department of Electrical and Computer Engineering, University of Southern California, Los Angeles, CA, USA. [4]These authors contributed equally: Midya Parto, William Hayenga. ✉e-mail: khajavik@usc.edu

Realizing spin-Hamiltonians in nanoscale active photonic lattices

Midya Parto[1†], William Hayenga[1†], Alireza Marandi[2], Demetrios N. Christodoulides[1] & Mercedeh Khajavikhan[1,3*]

[1]CREOL, The College of Optics and Photonics, University of Central Florida, Orlando, FL 32816-2700, USA.
[2]Department of Electrical Engineering, California Institute of Technology, Pasadena, CA 91125, USA
[3]Ming Hsieh Department of Electrical and Computer Engineering, University of Southern California, Los Angeles, California 90089, USA

*Corresponding Author: khajavik@usc.edu
†These authors contributed equally to this work.

SUPPLEMENTARY INFORMATION

Part 1. Derivation of the energy landscape function

In order to obtain the resonant modes supported by the nanodisks, we consider the two general sets of transverse electric (TE) and transverse magnetic (TM) modes. Using separation of variables, and after solving the Helmholtz equation in cylindrical coordinates, one finds the field components for TE_{nm} modes in a nanodisk at site j as

$$\begin{gathered}
E_{\rho,j} \propto \frac{n}{\rho} J_n(k_\rho \rho)\, sin(n\phi + \phi_j), \\
E_{\phi,j} \propto \frac{k_\rho}{2}\left[J_{n-1}(k_\rho \rho) - J_{n+1}(k_\rho \rho)\right] \cos(n\phi + \phi_j) \\
E_{z,j} = 0 \\
H_{\rho,j} \propto \frac{-\sqrt{k^2 - k_\rho^2} \times k_\rho}{2\omega\mu_0}\left[J_{n-1}(k_\rho \rho) - J_{n+1}(k_\rho \rho)\right] \cos(n\phi + \phi_j) \\
H_{\phi,j} \propto \frac{n\sqrt{k^2 - k_\rho^2}}{\omega\mu_0 \rho} J_n(k_\rho \rho) \sin(n\phi + \phi_j) \\
H_{z,j} \propto \frac{ik_\rho^2}{\omega\mu_0} J_n(k_\rho \rho) \cos(n\phi + \phi_j).
\end{gathered} \tag{S-1}$$

On the other hand, the expression for the total dissipated electromagnetic power due to the metallic walls can be obtained from the surface integrals

$$\mathcal{P}_{L,T} \propto \sum_{j=1}^{N} \int_{S_j} \left[\left|H_{\phi,j}\right|^2 + \left|H_{z,j}\right|^2 \right] ds$$
$$- \Delta S \sum_{j=1}^{N} \left\{ \left|H_{z,j}\right|^2 + \left|H_{z,j+1}\right|^2 - \left|H_{z,j+1} - H_{z,j}\right|^2 \right\} \quad \text{(S-2)}$$
$$+ \left\{ \left|H_{\phi,j}\right|^2 + \left|H_{\phi,j+1}\right|^2 - \left|H_{\phi,j+1} + H_{\phi,j}\right|^2 \right\},$$

where S_j is the cylindrical surface of the jth nanodisk, while ΔS is the effective common area between nearby nanodisks. From equations (S-1), one can further simplify equation (S-2) as follows

$$\mathcal{P}_{L,TE} \propto \mathcal{P}_1 - \mathcal{P}_{z,TE} \sum_{j=1}^{N} cos\left(j\frac{2\pi}{N}n + \phi_j\right) cos\left(-n\pi + j\frac{2\pi}{N}n + \phi_{j+1}\right)$$
$$+ \mathcal{P}_{\phi,TE} \sum_{j=1}^{N} sin\left(j\frac{2\pi}{N}n + \phi_j\right) sin\left(-n\pi + j\frac{2\pi}{N}n + \phi_{j+1}\right) \quad \text{(S-3)}$$

where $\mathcal{P}_{z,TE} = 2\Delta S \frac{k_\rho^4}{\omega^2\mu_0^2} J_n^2(k_\rho a)$, $\mathcal{P}_{\phi,TE} = 2\Delta S \frac{n^2(k^2-k_\rho^2)}{\omega^2\mu_0^2 a^2} J_n^2(k_\rho a)$, and a is the radius of the nanodisks. Equation (S-3) can be rewritten as

$$\mathcal{P}_{L,TE} \propto \mathcal{P}_1 + (-1)^{n+1} \sum_{j=1}^{N} \left\{ \frac{\mathcal{P}_{z,TE} - \mathcal{P}_{\phi,TE}}{2} cos\left[\phi_{j+1} - \phi_j\right] \right.$$
$$\left. + \frac{\mathcal{P}_{z,TE} + \mathcal{P}_{\phi,TE}}{2} cos\left[\phi_{j+1} + \phi_j + 2j \times \frac{2n\pi}{N}\right] \right\}. \quad \text{(S-4)}$$

Similarly, for TM_{nm} modes, the fields within cavities are given according to

$$E_{\rho,j} \propto \frac{-\sqrt{k^2 - k_\rho^2} \times k_\rho}{2\omega\epsilon_0} \left[J_{n-1}(k_\rho\rho) - J_{n+1}(k_\rho\rho)\right] cos(n\phi + \phi_j),$$
$$E_{\phi,j} \propto \frac{n\sqrt{k^2 - k_\rho^2}}{\omega\epsilon_0\rho} J_n(k_\rho\rho)\, sin(n\phi + \phi_j)$$
$$E_{z,j} \propto \frac{ik_\rho^2}{\omega\epsilon_0} J_n(k_\rho\rho)\, cos(n\phi + \phi_j) \quad \text{(S-5)}$$
$$H_{\rho,j} \propto -\frac{n}{\rho} J_n(k_\rho\rho)\, sin(n\phi + \phi_j)$$
$$H_{\phi,j} \propto -\frac{k_\rho}{2} \left[J_{n-1}(k_\rho\rho) - J_{n+1}(k_\rho\rho)\right] cos(n\phi + \phi_j)$$
$$H_{z,j} = 0.$$

Therefore, the total dissipated power can again be obtained in a similar way:

$$\mathcal{P}_{L,TM} \propto \mathcal{P}_2 + \mathcal{P}_{\phi,TM} \sum_{j=1}^{N} cos\left(j\frac{2\pi}{N}n + \phi_j\right) cos\left(-n\pi + j\frac{2\pi}{N}n + \phi_{j+1}\right), \quad \text{(S-6)}$$

where $\mathcal{P}_{\phi,TM} = \frac{k_\rho^2}{2}\Delta S\left[J_{n-1}(k_\rho\rho) - J_{n+1}(k_\rho\rho)\right]^2$. Using this, it is straightforward to show that

$$\mathcal{P}_{L,TM} \propto \mathcal{P}_2 + (-1)^n \mathcal{P}_{\phi,TM} \sum_{j=1}^{N} \left\{ \frac{1}{2} cos\left[\phi_{j+1} - \phi_j\right] + \frac{1}{2} cos\left[\phi_{j+1} + \phi_j + 2j \times \frac{2n\pi}{N}\right] \right\}. \quad \text{(S-7)}$$

Equations (1) and (2) in the main text can be directly extracted from (S-3), (S-6) and (S-4), (S-7), respectively. These equations provide the energy landscape functions associated with the Hamiltonians of this system.

In order to see how the energy landscape function can represent an anisotropic XY Hamiltonian, one can rewrite equation (S-3) in the following form:

$$\begin{aligned} \mathcal{P}_{L,TE} \propto \mathcal{P}_1 - \mathcal{P}_{z,TE} \times (-1)^n \textstyle\sum_{j=1}^{N} \left\{ \left[\cos j \frac{2\pi n}{N} \cos\phi_j - \sin j \frac{2\pi n}{N} \sin\phi_j \right] \times \right. \\ \left. \left[\cos j \frac{2\pi n}{N} \cos\phi_{j+1} - \sin j \frac{2\pi n}{N} \sin\phi_{j+1} \right] \right\} + \mathcal{P}_{\phi,TE} \times (-1)^n \textstyle\sum_{j=1}^{N} \left\{ \left[\sin j \frac{2\pi n}{N} \cos\phi_j + \right. \right. \\ \left. \left. \cos j \frac{2\pi n}{N} \sin\phi_j \right] \times \left[\sin j \frac{2\pi n}{N} \cos\phi_{j+1} + \cos j \frac{2\pi n}{N} \sin\phi_{j+1} \right] \right\} = \mathcal{P}_1 - \mathcal{P}_{z,TE} \times \\ (-1)^n \textstyle\sum_{j=1}^{N} \left\{ \cos^2 \frac{2\pi nj}{N} \cos\phi_j \times \cos\phi_{j+1} + \sin^2 \frac{2\pi nj}{N} \sin\phi_j \times \sin\phi_{j+1} - \frac{1}{2} \sin \frac{4\pi nj}{N} \sin(\phi_j + \right. \\ \left. \phi_{j+1}) \right\} + \mathcal{P}_{\phi,TE} \times (-1)^n \textstyle\sum_{j=1}^{N} \left\{ \sin^2 \frac{2\pi nj}{N} \cos\phi_j \times \cos\phi_{j+1} + \cos^2 \frac{2\pi nj}{N} \sin\phi_j \times \sin\phi_{j+1} + \right. \\ \left. \frac{1}{2} \sin \frac{4\pi nj}{N} \sin(\phi_j + \phi_{j+1}) \right\}. \end{aligned} \quad \text{(S-8)}$$

After rearranging, one would obtain

$$\begin{aligned} &\mathcal{P}_{L,TE} \propto \\ &= \mathcal{P}_1 + (-1)^n \sum_{j=1}^{N} \left\{ \left[\mathcal{P}_{\phi,TE} \sin^2 \frac{2\pi nj}{N} - \mathcal{P}_{z,TE} \cos^2 \frac{2\pi nj}{N} \right] \cos\phi_j \times \cos\phi_{j+1} \right. \\ &\quad + \left[\mathcal{P}_{\phi,TE} \cos^2 \frac{2\pi nj}{N} - \mathcal{P}_{z,TE} \sin^2 \frac{2\pi nj}{N} \right] \sin\phi_j \times \sin\phi_{j+1} \\ &\quad \left. + \frac{1}{2} \sin \frac{4\pi nj}{N} \left[\mathcal{P}_{\phi,TE} - \mathcal{P}_{z,TE} \right] \sin(\phi_j + \phi_{j+1}) \right\}. \end{aligned} \quad \text{(S-9)}$$

From here, one would obtain

$$\mathcal{H} = \sum_{j=1}^{N} \left\{ J_{x,j} \sigma_{x,j} \sigma_{x,j+1} + J_{y,j} \sigma_{y,j} \sigma_{y,j+1} + \vec{\sigma}_j . \mathbf{\Gamma}_{j,j+1} . \vec{\sigma}_{j+1}^{T} \right\} = \mathcal{H}_{XY} + \mathcal{H}_0, \quad \text{(S-10)}$$

where $J_{x,j} = (-1)^n \left(\mathcal{P}_{\phi,TE} \sin^2 \frac{2\pi nj}{N} - \mathcal{P}_{z,TE} \cos^2 \frac{2\pi nj}{N} \right)$, $J_{y,j} = (-1)^n \left(\mathcal{P}_{\phi,TE} \cos^2 \frac{2\pi nj}{N} - \mathcal{P}_{z,TE} \sin^2 \frac{2\pi nj}{N} \right)$ and

$$\mathbf{\Gamma}_{j,j+1} = \frac{1}{2} \sin \frac{4\pi nj}{N} (-1)^n \left[\mathcal{P}_{\phi,TE} - \mathcal{P}_{z,TE} \right] \begin{bmatrix} 0 & 1 \\ 1 & 0 \end{bmatrix}. \quad \text{(S-11)}$$

It is evident from equation (S-11) that if $4n/N = m$ is an integer, then the equivalent spin Hamiltonian associated with this energy landscape function reduces to the XY Hamiltonian with a lifted U(1) symmetry.
Similar results can be obtained for TM modes.

Part 2. Fabrication procedure and SEM images

The fabrication steps involved in implementing metallic nanolaser lattices are depicted below in Fig. S1. The wafer (grown by OEpic Inc.) consists of six quantum wells

of $In_{x=0.734}Ga_{1-x}As_{y=0.57}P_{1-y}$ (thickness: 10 nm), each sandwiched between two cladding layers of $In_{x=0.56}Ga_{1-x}As_{y=0.938}P_{1-y}$ (thickness: 20 nm), with an overall height of 200 nm, grown on an InP substrate. The quantum wells are covered by a 10 nm thick InP over-layer for protection (Fig. S1a). An XR-1541 hydrogen silsesquioxane (HSQ) solution in methyl isobutyl ketone (MIBK) is used as a negative electron beam resist. The resist is spun onto the wafer, resulting in a thickness of 50 nm (Fig. S1b). The lattices are then patterned by electron beam lithography (Fig. S1c). The wafer is next immersed in tetramethylammonium hydroxide (TMAH) to develop the patterns. The HSQ exposed to the electron beam now remains and serves as a mask for the subsequent reactive ion etching process. To perform the dry etching, a mixture of H_2:CH_4:Ar gas is used with a ratio of 40:6:15 sccm, RIE power of 150 W, and ICP power of 150 W at a chamber pressure of 35 mT (Fig. S1d). The wafer is then cleaned with oxygen plasma to remove organic contaminations and polymers that form during the dry etching process. After this, a 1000 nm layer of silver is deposited onto the sample using electron beam evaporation at a pressure of 5×10^{-7} Torr at a rate of 0.1 $\dot{A}/s$ for the first 400 nm, at which point the rate is ramped up to 1 $\dot{A}/s$ (Fig. S1e). SU-8 is then used to bond the silver side to a glass substrate for support (Fig. S1f). Lastly, the sample is wet etched in hydrochloric acid to remove the InP substrate (Fig. S1g). SEM images of all lattices discussed in the main text are provided in Fig. S2, after the intermediate dry etching step.

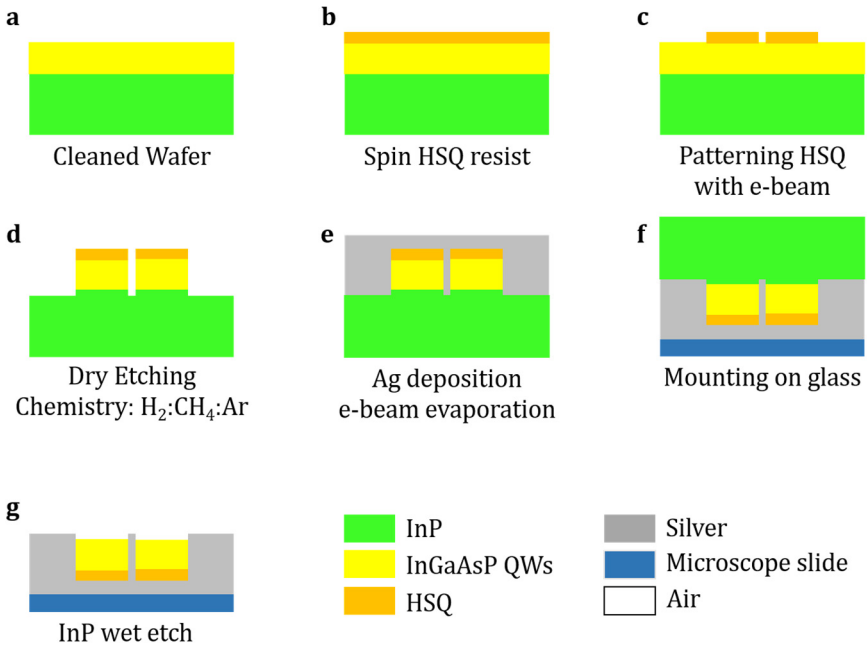

Fig. S1| Fabrication process of a metallic nanolaser lattice. This same process is used in other geometries as well. The bottom right corner provides a legend to the materials of the structure. **a,** Cleaned wafer with InGaAsP quantum wells grown on an InP substrate. **b,** A thin layer of negative tone HSQ ebeam resist is spun onto the sample. **c,** The wafer is patterned by ebeam lithography and the resist is developed. **d**, A dry etching process is used to define the lattice. **e,** 1 μm Ag is deposited by means of ebeam evaporation. **f,** The sample is mounted and bonded to a glass microscope slide silver side down with SU-8. **g,** Sample is immersed into HCl to remove the InP substrate.

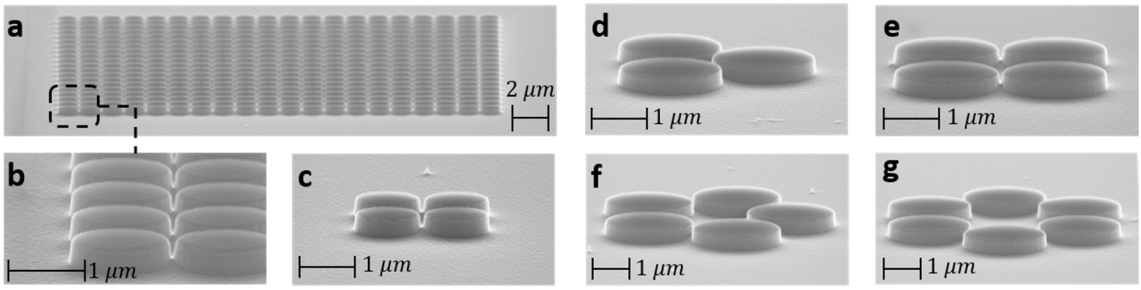

Fig. S2| SEM images of the lattices. In all lattices the nanodisks elements are separated by 50 nm. **a,** 20 x 20 array of nanodisks (radius 545 nm). **b,** zoomed in view of the front left corner of the 20 x 20 array. **c,** 4-element array of nanodisks (radius 575 nm). **d, e, & f**, 3-, 4-, & 5-element arrays (radius 930 nm, 940 nm, and 930 nm, respectively). **g,** 6-element array (radius 850 nm).

Part 3. Characterization setup schematic

A micro-photoluminescence (μ-PL) setup, depicted in Fig. S3, is used to characterize

the metallic nanolaser lattices. The lattices are optically pumped by a pulsed laser (duration: 15 ns, repetition rate: 290 kHz) operating at a wavelength of 1064 nm (SPI fiber laser). A beam shaping system is implemented to realize the desired pump profile. In this study, the pump focus spot on the sample has a diameter of 45 μm. A 50x microscope objective (NA: 0.42) is used to project the pump beam on the lattice and also serves to collect the emission. For temperature tuning, the sample is inserted into a cryostat (Janis ST-500) and cooled. The surface of the sample is imaged by two cascaded 4-f imaging systems in an IR camera (Xenics Inc.). A broadband ASE source passed through a rotating ground glass is used to illuminate the sample surface for pattern identification. A notch filter is placed in the path of emission to attenuate the pump beam. Output spectra are obtained by a monochromator equipped with an attached InGaAs linear array detector. A powermeter is inserted at the focus of the beam to collect the output power of the laser lattices. A linear polarizer is placed in the setup to observe the polarization resolved intensity distribution. To measure the topological charge of the light emitted by the lattices, a removable equilateral triangular aperture is inserted at the back focal plan of the lens before the IR camera, to facilitate a Fourier-transform. A quarter-wave plate is used to extract the right- and left-handed components of the polarization.

To measure the orbital angular momentum of the emitted light emitted, different techniques can be used based on interference, including self-interference and interference of the OAM beam with a plane wave. In these circumstances, the phase information is assessed by analyzing the fringes. In particular, the formation of a fork-like structure at the center of the vortex is an indication of a topological charge. Here the topological charge measurements are augmented using a different approach based on the relationship between the phase of the light carrying OAM and its diffraction (ref. [34] of the main text). This latter technique provides an unambiguous measurement of the order and sign of a vortex beam's topological charge. In short,

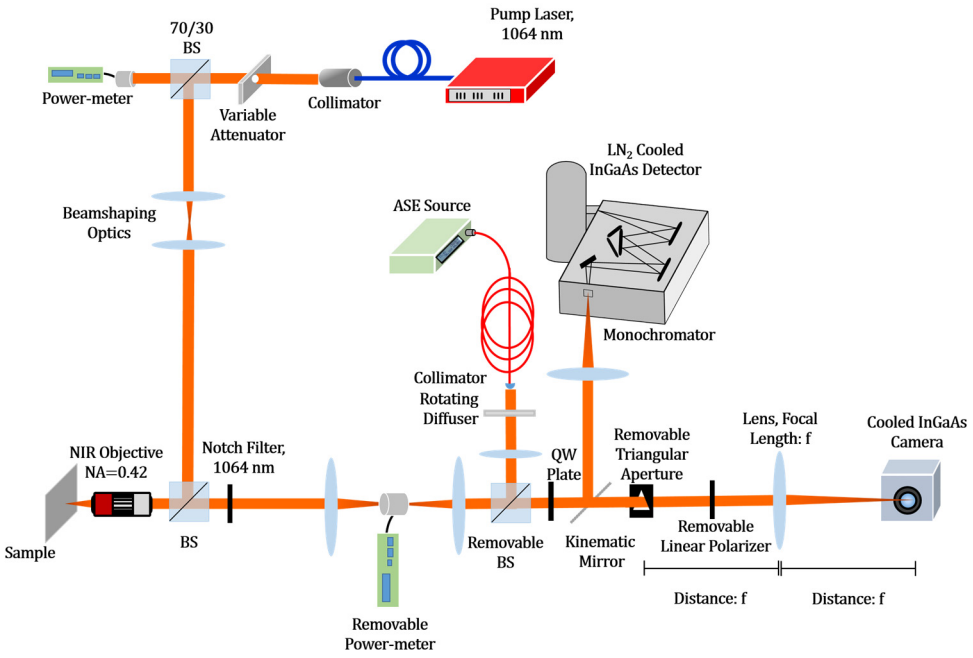

Fig. S3| Characterization microphotoluminescence setup schematic. The samples are pumped with a 1064 nm fiber laser and focus onto the sample with a 50x objective (N.A. 0.42). Light is either directed to an InGaAs camera to observe emission patterns, or to a monochromator with an attached InGaAs linear array detector. The emission power is collected at the location of the first focus after the pump notch filter. The triangular aperture used to reveal the OAM of the radiated beams is removable so as to not obstruct imaging the sample surface and to collect proper modal profiles.

when a *scalar* light beam carrying orbital angular momentum passes through an equilateral triangular aperture, the beam diffracts, hence generating a truncated triangular optical lattice rotated by $\pm 30°$, with respect to the aperture, in the far-field. This lattice then reveals the value of the topological charge (q), given by the relationship $|q| = s - 1$, where s is the number of spots along each side of the formed triangular lattice. The sign of the charge is determined by the direction that the triangle rotates. For example, in our setup, a triangle pointed right has a positive OAM, while the sign is negative if it points left.

To establish the validity of the triangular aperture approach for measuring the topological charge of an optical vortex beam, we compare the results of the triangle technique experimentally to that of a simulated vectorially rotating electric field. In the experiment, we tested a 7-element lattice laser at room temperature (Fig S4 a). As the TE_{13} is a quasi-linear like mode, we simulate this structure by considering six dipoles arranged in a hexagonal ring, emitting radiation with an electric field $\vec{E} \propto -\cos(2\varphi)\,\hat{x} + \sin(2\varphi)\,\hat{y}$, where φ is the angle of rotation along the periphery. This in

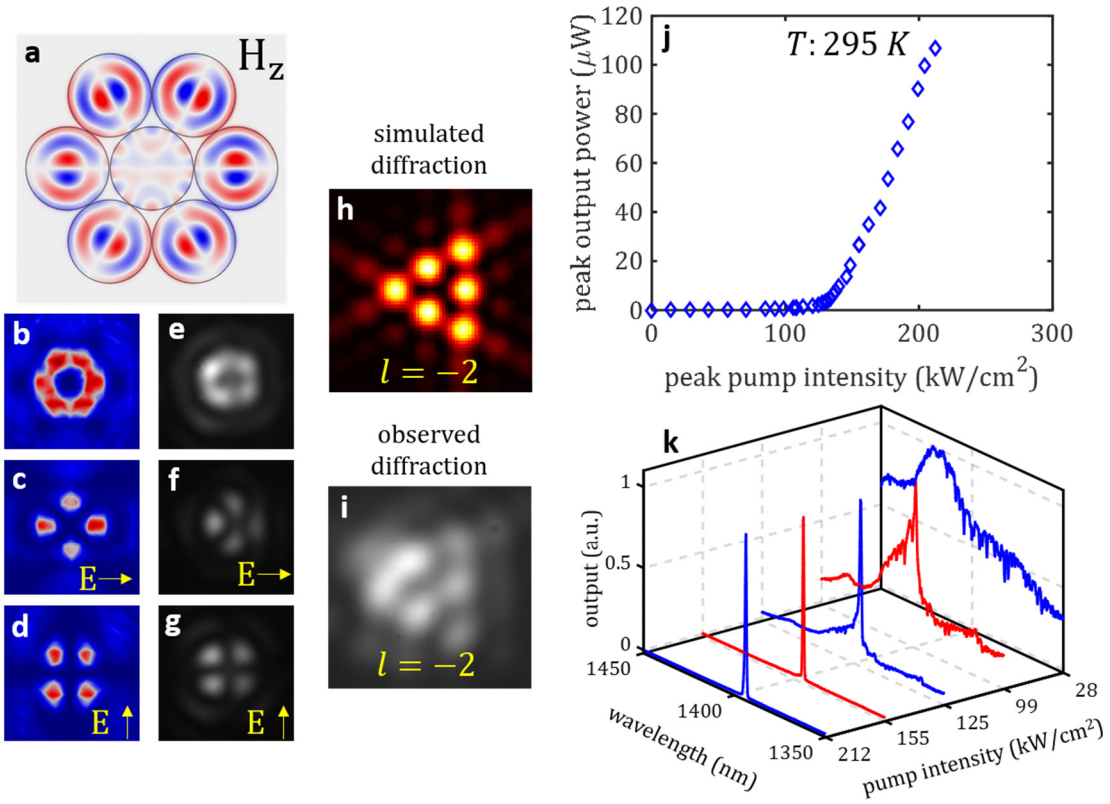

Fig. S4| Characterization of charge measurement using a 7-element metallic lattice operating at room temperature. a, Simulated z-component of the magnetic field. **b, c, & d,** The simulated intensity profile and the polarization resolved intensity distributions when filtered for horizontal (**c**) and vertical (**d**) polarizations. **e, f, & g,** The experimentally observed emission pattern and intensity distributions. **h,** The simulated far-field diffraction pattern of the lattice after passing through a triangular aperture. **i,** The experimentally observed profile is in agreement and has $l = -2$. **j,** The light-light curve shows a clear onset in lasing. **k,** The spectral evolution of this laser shows linewidth narrowing and single-mode behavior.

turn can be represented in terms of left- ($\hat{L}$) and right-hand circular polarizations ($\hat{R}$)(L,RHCP), $\vec{E} \propto -e^{i2\varphi}\hat{L} - e^{-i2\varphi}\hat{R}$. Figures S4 b, c, & d provide the simulated intensity and the polarization resolved intensity distributions, which are in excellent agreement with the observed modal profiles (Fig. S4, e, f, & g). Figure S4 h shows the result of the simulated diffraction pattern when filtering for the RHCP, and compares it to the experimentally observed diffraction profile (Fig. S4 i). Lastly, the associated light-light (L-L) and spectral evolution curves are provided in Fig. S4, j & k, respectively, clearly showing the threshold characteristic associated with lasing as well as linewidth narrowing.

Part 4. Light-light curves and spectral evolutions

In addition to the emission profile and topological charges provided in the main text, light-light and spectral evolution curves were also collected for these metallic nanolaser lattices. As mentioned before, the ambient temperature of the lasers was tuned in order to promote lasing in certain desired modes. All of the curves shown in this section of the supplementary display a threshold and a linewidth narrowing behaviors with increased pumping, attributes associated with lasing. The reported pump intensities represent the incident light at the sample surface.

Figure S5 provides the L-L and spectral evolutions of the four lattices that orient their fields in an antiferromagnetic-like arrangement. The 3-, 4-, & 5-element structures have individual element radii of 930 nm, 940 nm, and 930 nm, respectively, (TE_{14}

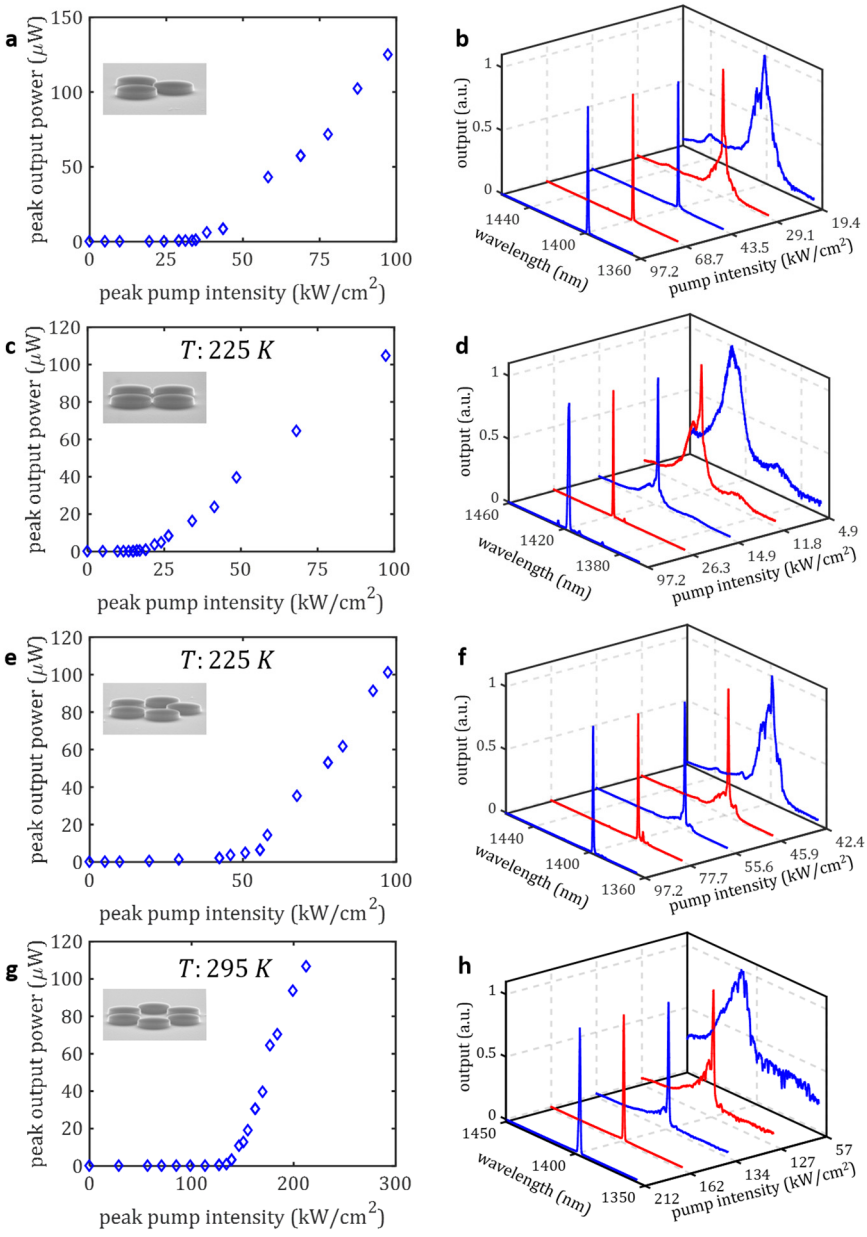

Fig. S5| Light-light and spectral evolutions curves for the lattices with antiferromagnetic-like coupling. All the lattices indicate a clear onset of lasing and linewidth narrowing. **a & b, c & d, and e & f,** show the light-light and the spectral evolutions of lattices operating in the TE_{14} mode at temperature of 225 K for the 3-, 4-, & 5-element lattices, respectively. The radii of the nanodisks are 930 nm, 940 nm, and 930 nm, respectively. **g & h** the 6-element lattice supports lasing at room temperature in the TE_{13} mode (850 nm radius elements) [1-4].

mode) and are tuned to a temperature of 225 K (Fig. S5 a-f). On the other hand, the 6-element lattice (nanodisk radius of 850 nm) is left at room temperature to promote lasing in the TE_{13} mode (Fig. S5 g & h).

Figure S6 shows the curves for the lattices that orient their fields in a ferromagnetic-like manner. In these lattices all the cavities support the TE_{22} mode. The 4-element arrangement operates at a temperature of 78 K and the characteristics of the L-L and spectral evolution (575 nm nanodisk radius) is provided in Fig. S6 a & b. In the case of the 20 × 20 element array, the nanodisks have a smaller radius of 545 nm and were operated at an ambient temperature of 225 K (Fig. S6 c & d).

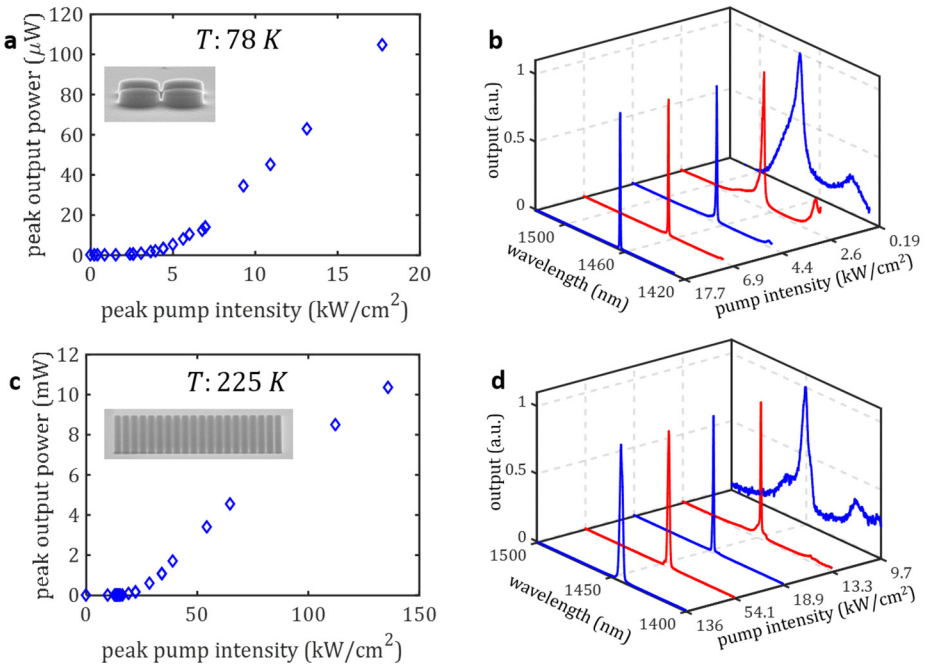

Fig. S6| Output charactersitics of the 4-element and 20×20-element array displaying ferromagnetic like coupling. Both lattices operate in the TE_{22} mode, albeit at differing temperatures. **a & b,** the 4-element arrangement is cooled to 78 K and has disks with radii of 575 nm. **c & d**, the 20 × 20-element lattice (radius of 545 nm) generates more than 10 mW peak output power [5, 6].

Part 5. Tuning the exchange couplings J_{ij}

In order to show the versatility of the coupled nanolaser array platform to realize XY Hamiltonians with various exchange couplings, one may consider varying the metallic gap between nanodisks as a means to adjust the associated exchange couplings in equation (2). To demonstrate this aspect, we study an asymmetric three-element configuration, as depicted schematically in Fig. S7 a. In this configuration, we adjust the relative strengths of the corresponding exchange couplings in the equivalent Hamiltonian of equation (2) such that $J_{12} = J_{13} \approx J_{23}/3$. This is obtained by incorporating a larger gap distance between the top nanodisk and the remaining ones on the bottom of the structure (50 nm versus 25 nm). Each of the nanodisks in this case have a radius of 775 nm and emit in the TE_{13} mode. In this case, one expects that the previous 120° arrangement of the pseudospins in an equilateral geometry to be

modified towards an anti-aligned pseudospin configuration for the sites located on the bottom of the triangle, as expected from the limiting case of an AF-like coupled dimer geometry. Figure S7 b shows simulated field profile of the associated supermode with the lowest loss in such a geometry, as expected from such asymmetric couplings. Figures S7 c-h display the measured diffracted field intensities and polarization characteristics of light emitted by such a structure (top) together with the associated simulation results (bottom). The coupling between the adjacent elements can be further tuned by depositing additional metallic barriers using focused ion beams.

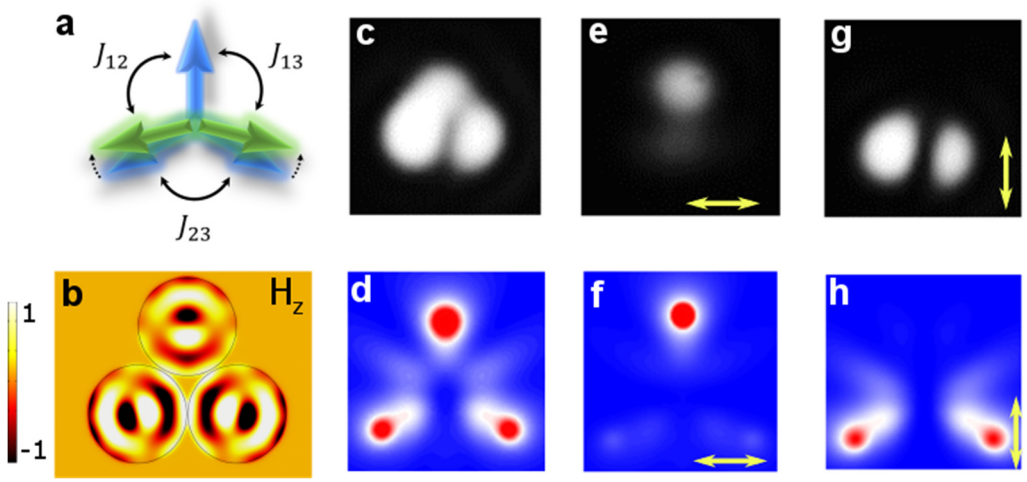

Fig. S7| Asymmetric triangle geometry. a, A schematic of three pseudospins arranged on a triangle with asymmetric exchange couplings. In this case, the angles of the bottom pseudospins are expected to change as shown in the figure. **b,** FEM simulation of the lasing supermode in an asymmetric triangular array of nanodisks. Each nanodisk supports a TE_{13} mode. **c-h** Experimental measurements (top) together with theoretically calculated results for diffraction intensities and polarization states of the optical fields emitted by such a nanodisk array. The arrows depict the direction of the linear polarizer.

Part 6. Polarization measurements for frustrated states

To further characterize the lasing supermodes in the case of arrays with $N = 3, 5, 6$ nanodisk lasers with an AF-type coupling, we performed polarization measurements in each case and compared the results with those expected from simulations (Fig. S8). These observations further corroborate the results in Fig. 4 of the manuscript.

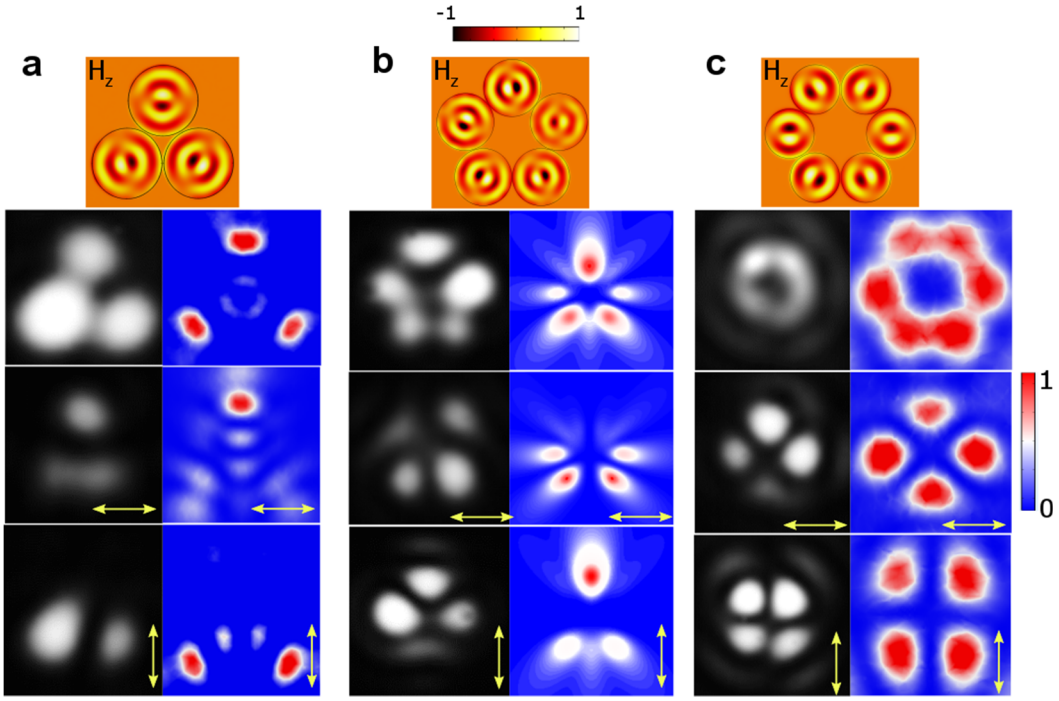

Fig. S8| Polarization measurements for frustrated states. Theoretically predicted and experimentally measured polarization profiles for lasing supermodes in arrays of **a,** $N = 3$, **b,** $N = 5$, and **c,** $N = 6$ nanodisk laser arrays**.** The arrows indicate the direction of linear polarizations.

Part 7. Characterization of single element nanolasers

To gain a deeper insight into the behavior of various arrays of nanolasers, and to assure the absence of any multimode lasing in the individual elements, we carefully characterized several single element nanolasers, fabricated in various sizes and geometries (nanodisk as well as coaxial). Figure S9 shows simulated resonant modes with highest quality factors of nanodisks with different radii (545 and 930 nm, as used in the FM and AF arrangements throughout this study). In both cases, only one highly confined mode coincides with the gain bandwidth of the quantum well system. Experimental results obtained from these elements are also provided in the same figure, clearly showing single mode lasing based their emitted spectra. Figure S10 further shows additional measured spectra from other nanolaser single elements. In all the cases studied, consistent single-mode lasing was observed.

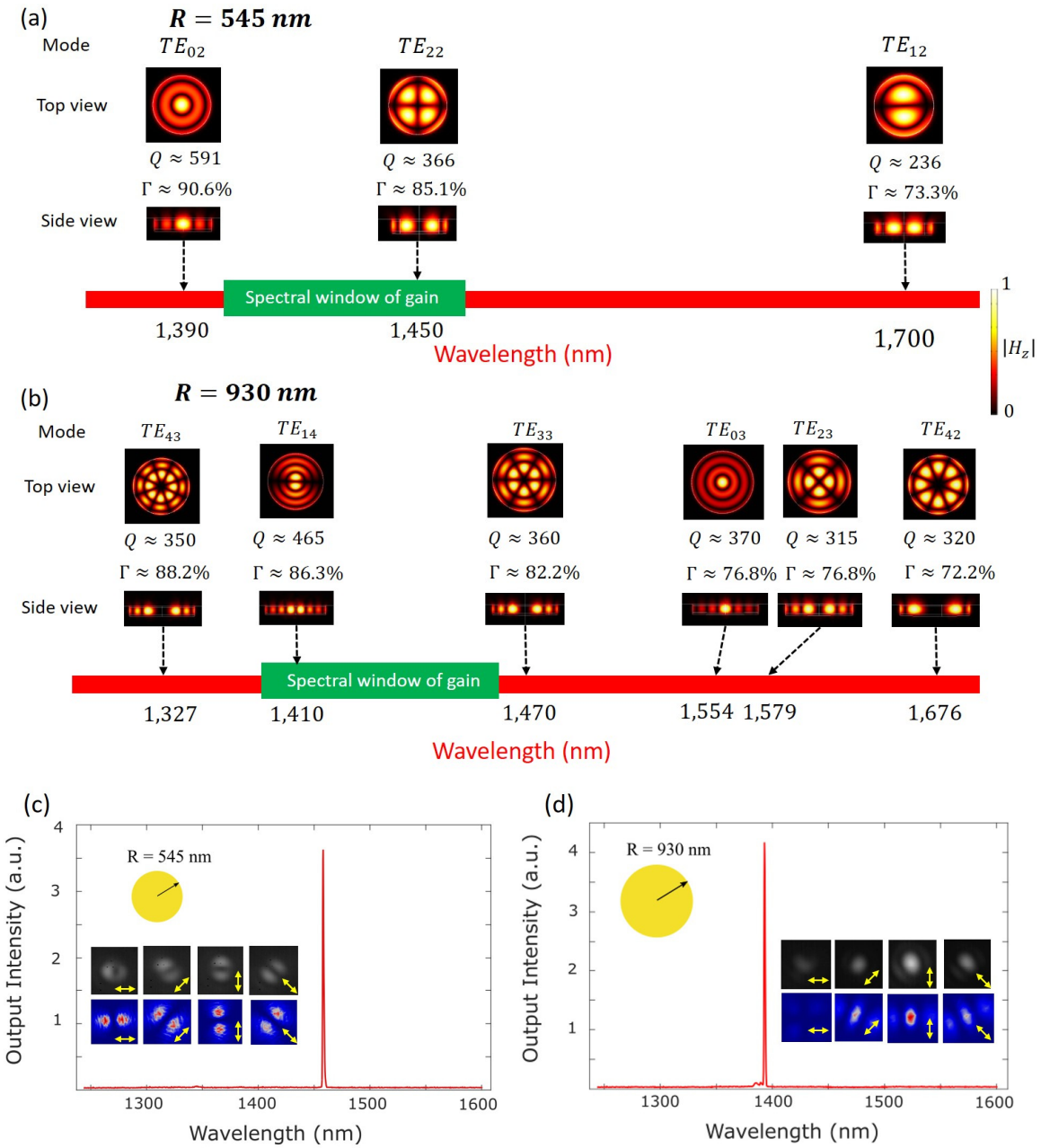

Fig. S9| Resonance spectra and mode profiles associated with the highly confined modes of a single nanodisk laser. Nanolaser elements used in (a) FM ($R = 545\,nm$) and (b) AF ($R = 930\,nm$) experiments, at a temperature of 225 K. In each case, Q is the quality factor and Γ is the gain confinement factor. These results explain the single-mode lasing of the TE_{22} mode (case (a)) and TE_{14} mode (case (b)) in each scenario. Measured emitted spectra from single nanolasers corresponding to (a, b) are depicted in (c, d) respectively. The insets in (c, d) indicate simulated as well as measured diffraction intensities and polarization states.

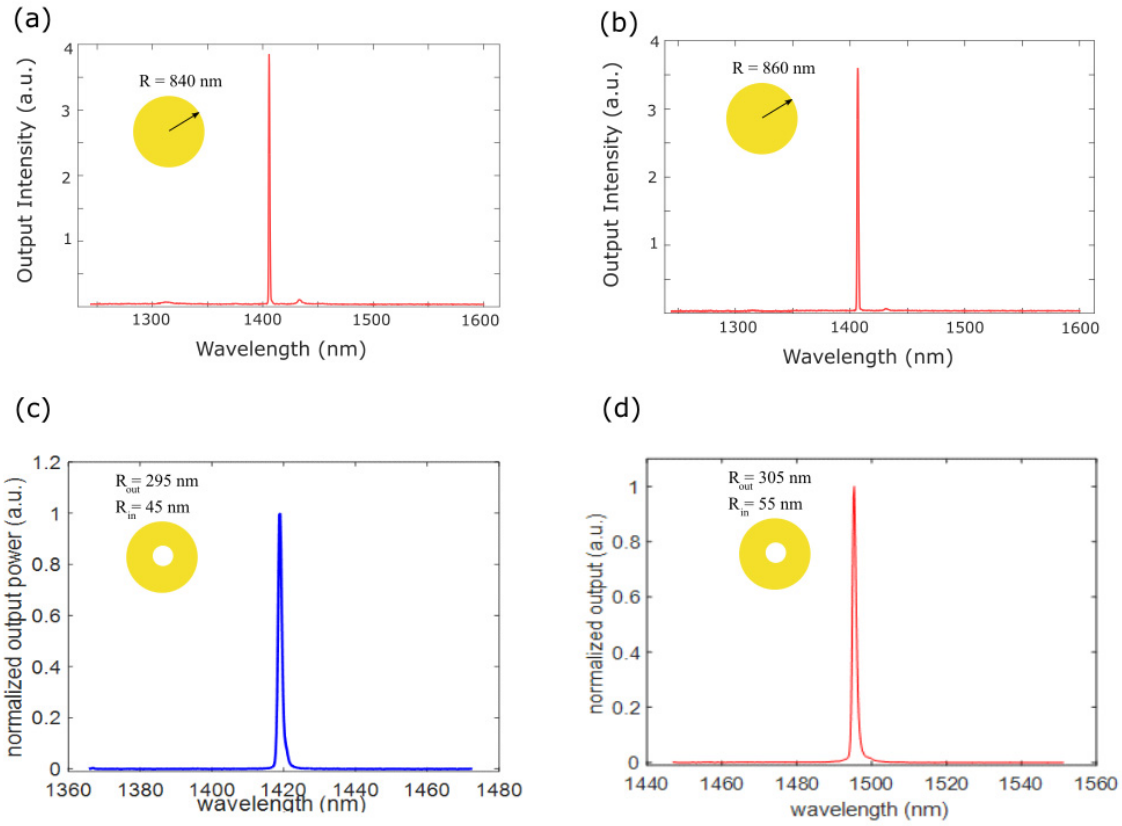

Fig. S10| Single mode lasing action within various nanolaser elements. Emitted light spectra from (a, b) nanodisks and (c, d) coaxial nanolasers with different sizes [7, 8].

Part 8. Lasing in the TE_{0m} and TM_{0m} modes

We considered using $TE_{0\mathrm{m}}$ and $TM_{0\mathrm{m}}$ modes of coaxial metallic nanolasers (Fig. S11) to realize Ising Hamiltonian in these platforms. Our preliminary simulations show that by using these modes it is possible to implement both FM and AF exchange interaction terms in the Ising Hamiltonian. This is evident from Eqs. (S-3) and (S-6), which in the case of $n = 0$ become:

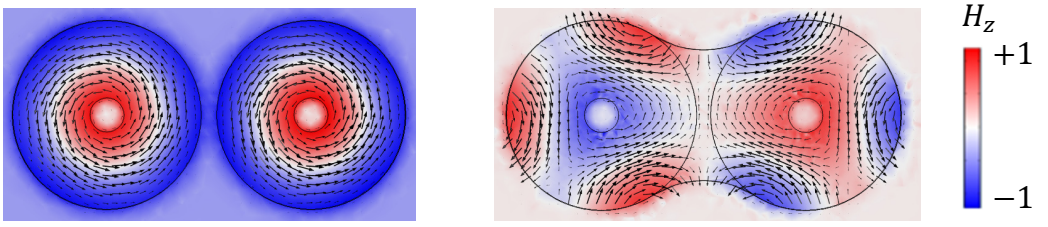

Fig. S11| Lasing in the TE_{0m} and TM_{0m} modes of nanolasers. Two coupled metallic coaxial nanolasers operating in a TE_{01} mode, exhibiting an FM (left) and AF (right) exchange interaction between equivalent Ising pseudospins (spin up or down corresponds to clockwise/counterclockwise electric field vectors).

$$\mathcal{P}_{L,TE} \propto \mathcal{P}_1 - \mathcal{P}_{z,TE} \sum_{j=1}^{N} \cos\phi_j \cos\phi_{j+1} + \mathcal{P}_{\phi,TE} \sum_{j=1}^{N} \sin\phi_j \sin\phi_{j+1} \quad \text{(S-12)}$$

$$\mathcal{P}_{L,TM} \propto \mathcal{P}_2 + \mathcal{P}_{\phi,TM} \sum_{j=1}^{N} \cos\phi_j \cos\phi_{j+1} \quad \text{(S-13)}$$

In these scenarios, it can be directly seen from Eqs. (S-12, S-13) that the coupling between nearby lasers in this case is isotropic (independent of ϕ, i.e. the local azimuthal coordinate of each element), and hence any anisotropic terms (e.g. the H_0 term) is absent in the associated equivalent Hamiltonian. Moreover, one can check that the ground state associated with the energy landscape functions in these equations satisfy $\phi_{j+1} = \phi_j + m\pi$. By utilizing this latter property, we intend to use such $TE_{0\mathrm{m}}$ and $TM_{0\mathrm{m}}$ modes to emulate the Ising Hamiltonian in our nanolaser platform.

References

[1] https://doi.org/10.6084/m9.figshare.11796420
[2] https://doi.org/10.6084/m9.figshare.11796423
[3] https://doi.org/10.6084/m9.figshare.11796432
[4] https://doi.org/10.6084/m9.figshare.11796444
[5] https://doi.org/10.6084/m9.figshare.11796435
[6] https://doi.org/10.6084/m9.figshare.11796447
[7] https://doi.org/10.6084/m9.figshare.11796159
[8] https://doi.org/10.6084/m9.figshare.11796162